Article

RuNi-Supported TiO$_2$-Modified MgAl$_2$O$_4$ Catalyst for CO Selective Methanation in Hydrogen-Rich Gas

Qin Su and Xinfa Dong *

Guangdong Provincial Key Laboratory of Green Chemical Product Technology, School of Chemistry and Chemical Engineering, South China University of Technology, Guangzhou 510640, China; 202221024243@mail.scut.edu.cn
* Correspondence: cexfdong@scut.edu.cn

Abstract: CO selective methanation is regarded as an efficient technological solution for hydrogen-rich gas purification in fuel cells. In this study, a series of bimetallic catalysts (Ru-Ni/xTiO$_2$-MgAl$_2$O$_4$) were synthesized by impregnation method after surface modification of MgAl$_2$O$_4$ supports with different contents of TiO$_2$. The prepared catalysts were characterized by XRD, BET, SEM, TEM, H$_2$-TPR, CO-TPD, NH$_3$-TPD, and XPS. The Ru-Ni/10TiO$_2$-MgAl$_2$O$_4$ exhibited excellent CO-SMET performance, removing the CO in the H$_2$-rich gas to less than 10 ppm with the selectivity above 50% in a temperature window range of 210–280 °C. The results showed that the TiO$_2$-modified MgAl$_2$O$_4$ support not only improved the interaction between metal and support, and promoted the dispersion of active component nanoparticles on the support, but also introduced oxygen vacancies or defects in the catalyst and enhanced the acidity, resulting in better catalytic activity and stability.

Keywords: CO selective methanation; MgAl$_2$O$_4$; TiO$_2$-modified; Ni; Ru

1. Introduction

In the face of the increasingly serious environmental pollution energy crisis, it is a general trend to respond to use clean energy and implement the green and sustainable development of energy. The use of proton exchange membrane fuel cells (PEMFC) is regarded as the most promising energy conversion strategy due to its advantages of high energy efficiency, environmental protection, and low operating temperature [1,2]. However, the feedstock hydrogen-rich gas from hydrocarbon steam reforming contains about 0.5–2 vol% CO, which will irreversibly poison the Pt electrodes in the PEMFC, leading to a severe degradation of cell performance [3]. Therefore, the CO in the reforming hydrogen-rich gas must be deeply removed to a concentration of less than 10 ppm to ensure the efficient operation of the PEMFC [4].

The selective methanation of CO (CO-SMET) method is considered to be an effective chemical method [5] for deep CO removal due to its efficient conversion of CO to CH$_4$. The key is to develop CO-SMET catalysts with good low-temperature activity, high selectivity, good stability, and a wide temperature window.

Ni-Ru bimetal-supported catalysts are a class of CO-SMET catalysts that have attracted much attention due to their superior catalytic performance. It has been shown [6–8] that the incorporation of a small amount of Ru into the Ni-based catalyst can optimize the pore size structure of the catalyst, reduce the crystallite size of Ni, and improve its dispersion, thereby significantly improving the catalytic performance of the catalyst. Tada et al. [9,10] synthesized Ru-Ni/TiO$_2$ catalysts by the impregnation method and applied them to CO-SMET;

the results showed that the Ru-Ni/TiO$_2$ catalyst has better low-temperature activity as well as a wider temperature range compared with the monometallic catalysts. Ru can promote the reduction of metal Ni by spilling hydrogen, and this inter-metallic interaction improves the dispersibility and surface area of Ni and increases the active sites for CO methanation, thus improving the catalytic activity [11]. Yang et al. [12] showed that the doping of Ru is both kinetically and thermodynamically favorable to promote the decomposition of CO adsorbed on the Ni surface, thus enhancing the low-temperature activity and stability of the catalyst. Meanwhile, the choice of support also has an important influence on metal-loaded catalysts, and different combinations of active component and support exhibit different catalytic effects. Magnesia-aluminum spinel belongs to the typical cubic crystal system and has good thermal stability and sintering resistance [13]. Recent studies [14,15] have shown that magnesium-aluminum spinel can stabilize metal particles well, and reduces carbon buildup and metal nanoparticle aggregation even at high temperatures. In carbon monoxide catalytic hydrogenation reactions, the use of MgAl$_2$O$_4$ as a support can avoid the formation of a difficult-to-reduce NiAl$_2$O$_4$ structure from Ni and Al$_2$O$_3$, which leads to a decrease in the catalyst activity as well as the loss of the active component Ni [16]. Baek et al. [17] found that the self-activation property of Ru-promoted Ni/MgAl$_2$O$_4$ was the result of the simple combination of ruthenium self-activation ability and in situ reduction of nickel oxides by hydrogen transferred in the gas phase, which was the key for the catalyst to exhibit higher activity. Andraos et al. [18] showed that the reduced reduction temperature of NiO in Ru-Ni/MgAl$_2$O$_4$ catalyst promotes its dispersion, thereby exhibiting high activity and stability. Navarro et al. [19] reported that an MgAl$_2$O$_4$-supported Ru-Ni structured catalyst exhibited better reaction activity than MgO/Al$_2$O$_3$ for CO$_2$ methanation, increasing not only the CO$_2$ conversion but also decreasing the yield of the undesired product. However, MgAl$_2$O$_4$ support does not readily generate oxygen vacancies, which are critical for enhancing the adsorption and activation of CO molecules [20]. The interaction between active metal particles and MgAl$_2$O$_4$ is often weaker compared to other supports, which can result in the sintering of metal nanoparticles at high temperatures, leading to a loss of active surface area and reduced catalytic activity over time [21,22]. Moreover, it seems that MgAl$_2$O$_4$-based catalysts have poor low-temperature activity in CO-SMET, which tends to exacerbate CO$_2$ competition for the methanation reaction, thus leading to a decrease in reaction selectivity [23,24].

It has been shown that the incorporation of a TiO$_2$ additive into metal-supported catalyst can improve metal–support interactions and expose the acidic centers in the catalysts, and promotes the dispersion of the metal particles, thereby increasing the reactive active sites and enhancing the catalytic performance [25,26]. Titanium doping usually introduces oxygen vacancies or defects into the spinel structure of the support, which can facilitate the cleavage of C-O bonds and enhance the adsorption and activation of CO molecules, thereby increasing the catalytic activity [27]. Thus, in this paper, MgAl$_2$O$_4$ (tagged as MA) support was modified by TiO$_2$, and then Ru-Ni/TiO$_2$-MA catalyst was successfully constructed by the impregnation method. Compared with Ru-Ni/MA catalysts, the Ru-Ni/TiO$_2$-MA exhibits excellent metal dispersion and reducibility, and better CO adsorption activation ability, which improve the low-temperature activity and selectivity of the catalyst for CO-SMET.

2. Results and Discussion

Figure S1 shows the XRD spectra of xTiO$_2$-MA composite supports with different TiO$_2$ contents. It can be found that all of the modified samples exhibit the characteristic peaks of MA at 31.4°, 37.0°, 45.0°, 59.6°, and 65.5°, corresponding to the (220), (311), (440), (511), and (400) crystal planes (PDF #73-1959) [28]. The spectrum presents characteristic peaks of

different crystalline phases of Ti; the diffraction peaks at 25.2° and 53.5° are related to the reflection planes at (101) and (105) of anatase TiO_2 (PDF #71-1168), and the characteristic peaks were observed at 27.1° and 40.6°, which are related to the reflection planes at (110) and (111) of rutile TiO_2 (PDF #76-0326), respectively [29]. Compared with MA, the peak intensity of MA in the $xTiO_2$-MA (x = 5%, 10%, 15%) composites weakened with increasing TiO_2 content, where the TiO_2 characteristic peak intensity strengthened, indicating that TiO_2 crystals were formed on the surface of the support and encapsulated the MA [30]. The new crystalline phase peaks were not observed in XRD spectra of $xTiO_2$-MA, which suggested that titanium was not incorporated into the framework structure of MA.

Figure S2 and Table S1 show the N_2 absorption–desorption isotherms and pore size distribution results as well as the pore structure characterization of $xTiO_2$-MA with different TiO_2 contents. It can be seen in Figure S2 that the $xTiO_2$-MA exhibited the typical IUPAC type IV curves and H2 hysteresis loops, indicating the existence of a mesoporous structure of the supports, while the area of the hysteresis loops exhibited a decreasing trend with the elevation of the TiO_2 content, which suggests a consequent decrease in the mesoporous homogeneity and pore volume [31]. The Brunauer−Emmett−Teller (BET) surface area and average pore size for the $xTiO_2$-MA composite materials are summarized in Table S1. The pore distribution of all samples is between 6 and 7 nm, and the pore size is relatively uniform. The decrease in the specific surface area and the pore volume is due to the fact that part of the Ti did not enter into the frame pores of the MA supports, which has been confirmed by XRD test, but instead forms TiO_2 crystals on its surface [32].

Figure S3 presents the scanning electron microscope images of $xTiO_2$-MA and MA. It can be observed that all supports show irregular particle structure, and there is no obvious change in the morphology of MA before and after TiO_2 modification. $xTiO_2$-MA obviously distributes more tiny particles on the surface compared to MA, suggesting that titanium is uniformly loaded on the surface of MA to achieve the purpose of surface modification.

As indicated by the activity evaluation results of catalysts, when the loading amounts of TiO_2 was 10%, Ru-Ni/$10TiO_2$-MA exhibited excellent activity and selectivity over a wide reaction temperature window of 210–280 °C. As such, the role of additive TiO_2 and its influence on $10TiO_2$-MA-supported NiRu bimetallic catalysts will be investigated in the following.

The XRD patterns of the reduced samples of Ru-Ni/MA and Ru-Ni/$10TiO_2$-MA are displayed in Figure 1. The diffraction peaks at 44.5°, 51.8°, and 76.4° are related to the (111), (200), and (220) crystal planes of metallic Ni (PDF #87-0712) for both Ru-Ni/MA and Ru-Ni/$10TiO_2$-MA [33]. The characteristic peaks observed at 25.2° and 53.5° correspond to reflection planes at (101) and (105) of anatase TiO_2 (PDF #71-1168), and the characteristic peaks located at 27.1° and 40.6° are related to the reflection planes at (110) and (111) of rutile TiO_2 (PDF #76-0326) [29]. The characteristic diffraction peaks of Ru species were not observed, which may be due to the high dispersion of Ru [34]. The characteristic peaks at 37.0° and 65.5° correspond to the (311) and (400) crystal planes of MA (PDF #73-1959) [28]. The characteristic diffraction peaks at 62.3° for Ru-Ni/MA were related to the reflection planes at (220) of MgO (PDF#78-0430), which may be due to the low sintering temperature, resulting in unreacted magnesium sources existing in the form of MgO [35]. As shown in Figure 1, the diffraction peaks of $NiAl_2O_4$ were not observed, suggesting that the preparation process did not consume the active component Ni to generate difficult-to-reduce $NiAl_2O_4$. It can be observed that the (111) crystal plane diffraction peak of Ni for Ru-Ni/$10TiO_2$-MA was weakened in intensity compared with Ru-Ni/MA, indicating the particle size of the Ni for the Ru-Ni/$10TiO_2$-MA catalyst was smaller than that for the Ru-Ni/MA catalyst. The Ni particle sizes, estimated by the Scherrer equation [36], are listed in Table S2. These results suggested that the addition of an appropriate amount of

TiO_2 could effectively reduce the microcrystalline size of Ni. This result may be due to the fact that TiO_2 formed a strong metal–support interaction with Ni, which effectively inhibited the aggregation and growth of metal particles [29].
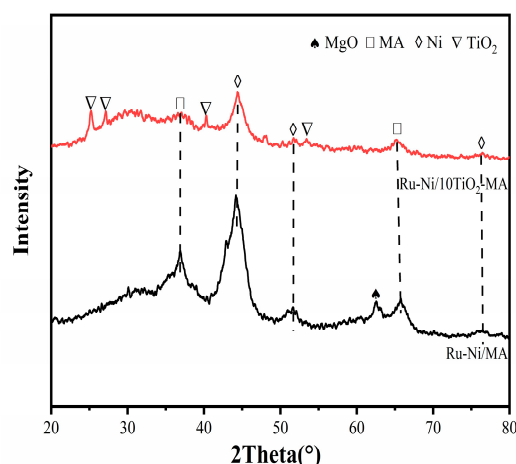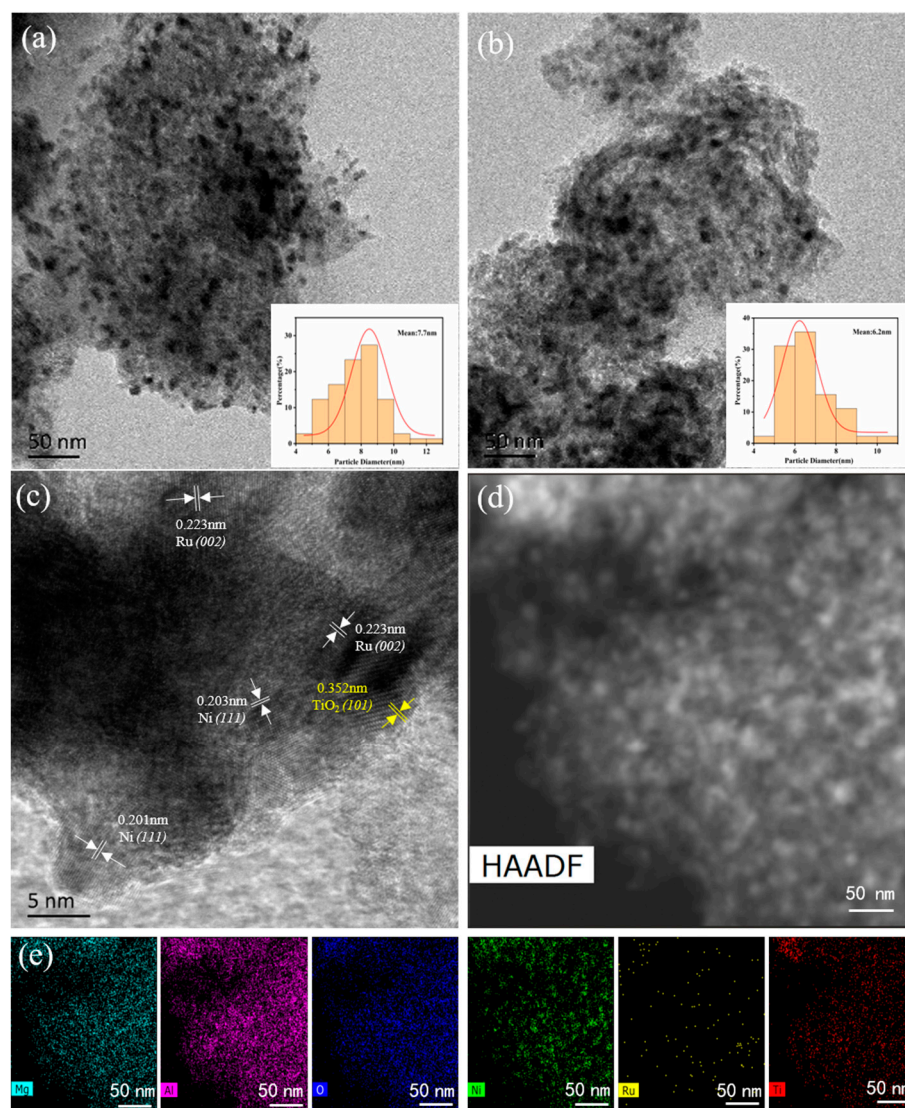

Figure 1. XRD patterns of Ru-Ni/MA and Ru-Ni/10TiO$_2$-MA catalysts.

As observed in Figure S2a, like the xTiO$_2$-MA supports, the Ru-Ni/10TiO$_2$-MA sample also presented the typical IUPAC type IV curves and H2 hysteresis loops, which suggested that the sample has a mesoporous structure [31]. As shown in Figure S2b and Table S2, the specific surface area, average pore volume, and the average pore diameter of Ru-Ni/10TiO$_2$-MA decreased compared to the support 10TiO$_2$-MA, suggesting that the number of the mesopores decreased with the addition of the active component, which was attributed to the fact that some of the mesopores are clogged or filled and transformed into smaller diameter pores.

The transmission electron microscopy (TEM) images of the catalyst and the particle size distribution of Ni are shown in Figure 2a,e. As presented in Figure 2a,b, the active metal Ni and Ru on support MA and 10TiO$_2$-MA, both dispersed and uniformly distributed in particle size, exhibited high dispersibility. The average sizes of the Ni and Ru nanoparticles for the Ru-Ni/MA and Ru-Ni/10TiO$_2$-MA catalysts are around 7.7 nm and 6.2 nm, respectively. The crystallite size of active metal for Ru-Ni/10TiO$_2$-MA decreased compared with Ru-Ni/MA, demonstrating that the introduction of TiO$_2$ was beneficial for reducing the particle size of the active components and improving its dispersion, which is conducive to creating more active sites for promoting the reaction [37]. It thus enhances the catalytic activity of Ru-Ni/10TiO$_2$-MA, which is consistent with the XRD results. It can be seen in Figure 2c that the lattice fringes at 0.20 nm, 0.22 nm, and 0.35 nm correspond to the (111) crystal planes of Ni, and the (002) crystal planes of Ru, and the (101) crystal plane of TiO$_2$, respectively [38,39]. The high-angle annular dark-field scanning transmission electron microscopy (HAADF-STEM) and EDX elementary mapping images of Ru-Ni/10TiO$_2$-MA are observed in Figure 2d,e, which indicated that the elements Ni, Ru, Ti, Mg, Al, and O were uniformly distributed over the entire catalyst surface.

Figure 2. TEM images and particle size distributions for (**a**) Ru-Ni/MA, (**b**) Ru-Ni/10TiO$_2$-MA, (**c**) HRTEM, and (**d**,**e**) HAADF-STEM and energy-dispersive X-ray (EDX) elemental mapping of Ru-Ni/10TiO$_2$-MA catalyst.

Figure 3 presents the H$_2$-TPR profiles of Ru-Ni /MA and Ru-Ni/10TiO$_2$-MA. The fractions of each type of NiO estimated from H$_2$-TPR experiments are summarized in Table S3. As shown in Figure 3 and Table S3, the samples exhibited obviously the reduction peaks of the Ru species at around 210 °C. For the Ru-Ni /MA catalyst, the reduction peak at 320 °C corresponds to α-NiO, which interacts weakly with the support MA, and the Ni particles are prone to form larger particle sizes after reduction. The reduction peaks at 350–400 °C correspond to β-NiO, and its interaction with the support is relatively strong, and the metal Ni particles obtained have excellent catalytic activity after β-NiO reduction. The peak at 515 °C corresponds to difficult-to-reduce γ-NiO [40,41]. For Ru-Ni/10TiO$_2$-MA, the α-NiO reduction peak shifted to 295 °C. The β-NiO reduction peak moves significantly to a low temperature and overlaps with the α-NiO reduction peak, and the peak area also increases significantly. This is because Ti modification improves the interaction between the active component and the support, forming more uniformly dispersed NiO particles, which is conducive to the reduction of NiO, especially β-NiO [42], which was beneficial for increasing the dispersion of active Ni species and improving the performance of the catalyst [43]. The peak area of the γ-NiO peak of Ru-Ni/10TiO$_2$-MA at

450 °C is significantly reduced, indicating that the addition of TiO_2 significantly reduces the amount of γ-NiO, which is difficult to reduce, thereby effectively increasing the active sites and enhancing the catalytic performance [44].
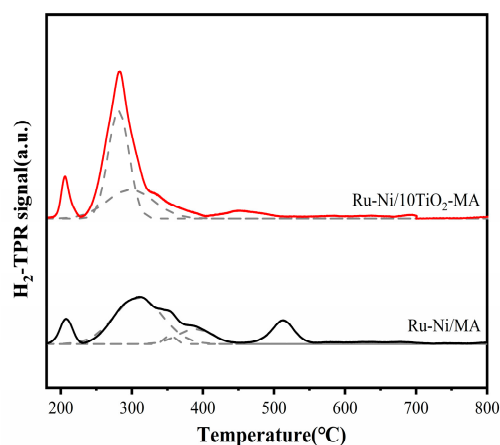
Figure 3. H_2-TPR profiles of the Ru-Ni/MA and Ru-Ni/$10TiO_2$-MA catalysts.

The CO-TPD curves of the catalysts are displayed in Figure 4. It can be observed that there are three peaks in the range of 50–600 °C for the Ru-Ni/MA and Ru-Ni/$10TiO_2$-MA catalysts. The CO desorption peaks at temperatures of 100 °C are assigned to the desorption of single-site CO chemisorption, and the desorption peaks in the range of 200–600 °C are attributed to the bridge chemisorption of CO, which contributes more to CH_4 formation than that of single-site CO chemisorption [45,46]. Compared with Ru-Ni/MA, the chemisorption peak area of single-site CO increased; the reason may be that the catalyst with proper amounts of TiO_2 has more exposed acidic sites and forms stronger chemical bonds with CO molecules, which in turn enhances the adsorption of CO [47]. The desorption peaks of the bridge-adsorption CO in the range of 200–600 °C for Ru-Ni/$10TiO_2$-MA shifted toward lower temperatures, indicating that the addition of TiO_2 reduced the adsorption strength of the catalyst for CO molecules, and this appropriate adsorption strength facilitated the adsorption and activation of CO molecules on the surface of the metal active sites [48]. Therefore, the methane reactivity of CO in CO-SMET was promoted and the performance of the catalyst was improved.
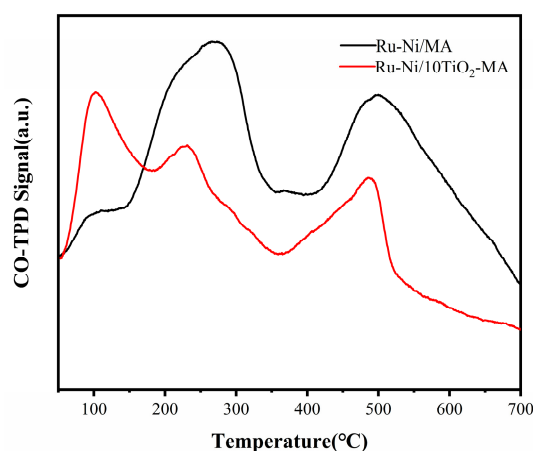
**Figure 4.** CO-TPD curves of the Ru-Ni/MA and Ru-Ni/$10TiO_2$-MA catalysts.

The NH_3-TPD profiles of the Ru-Ni/MA and Ru-Ni/$10TiO_2$-MA catalysts are exhibited in Figure 5. For Ru-Ni/MA, the low-temperature desorption peak located at 140 °C

represents the weak acid center, and the high-temperature peak at 500 °C is the strong acid center [49]. After the introduction of TiO_2, the weak acid desorption peak area of Ru-Ni/10TiO_2-MA was significantly increased, indicating that the amount of weak acid was enhanced. Interestingly, a new desorption peak corresponding to medium–strong acids was observed at 280 °C, indicating that the addition of TiO_2 increased the number of medium–strong acid sites, which was conducive to the adsorption and activation of CO molecules, thus improving the reaction performance [50]. The result can be attributed to the fact that the Ti^{4+} center acts as an electron acceptor and interacts with NH_3 molecules to enhance the Lewis acidity and provide more acidic sites for the catalyst [51]. The three desorption peaks above 400 °C were strong acid centers.
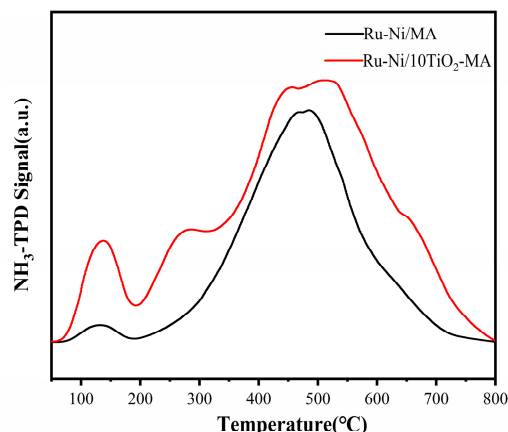
Figure 5. NH_3-TPD profiles of the Ru-Ni/MA and Ru-Ni/10TiO_2-MA catalysts.

Figure 6 shows the XPS spectra of Ru-Ni/MA and Ru-Ni/10TiO_2-MA catalysts. From the Ni $2p_{3/2}$ spectra in Figure 6a, both the Ru-Ni/MA and Ru-Ni/10TiO_2-MA catalysts presented three characteristic peaks situated at about 852 eV, 856 eV, and 862 eV, respectively, which were assigned to the binding energies of Ni^0 species, Ni^{2+} species, and the satellite peaks [52]. The characteristic peak of Ru species situated at around 461 eV was attributed to metallic Ru^0, suggesting that the RuO_x species is fully reduced. It is clear that the characteristic peaks of Ni^0 and Ni^{2+} species for the Ru-Ni/10TiO_2-MA catalyst were shifted towards the direction of low binding energies, while the Ru peak shifted to a higher binding energy compared to the Ru-Ni/MA catalyst. This result may be due to the synergistic effect between Ni and Ru that more electrons are transferred from Ru to Ni [53], or the increase in the metal electron cloud density induced by the strong interaction between the active metal and TiO_2 [54,55]. The production of more electron-rich Ni can weaken the C-O bonding of CO adsorbed on the Ni surface, which promotes the dissociation of CO and facilitates the methanation of CO [56,57]. For Ti species (Figure 6b), two characteristic peaks situated at 458.94 eV and 464.4 eV were observed, which corresponded to Ti $2p_{3/2}$ and Ti $2p_{1/2}$, indicating that the presence of Ti is mainly dominated by Ti^{4+}, which is the key to enhance the surface acidity of the catalyst and to promote C-O hydrogenolysis [30]. It can be seen from Figure 6c that the spectral signal with binding energy at 529.38 eV corresponds to the lattice oxygen of Ti^{4+} in TiO_2, and the characteristic peak located at 533.68 eV belongs to the defective oxygen resulting from the fact that structural distortion or defective oxygen exists in voids [58–60]. The phenomenon of increased defective oxygen in the Ru-Ni/10TiO_2-MA catalyst apparently facilitates the adsorption of CO, which in turn promotes the CO methanation reaction [27].
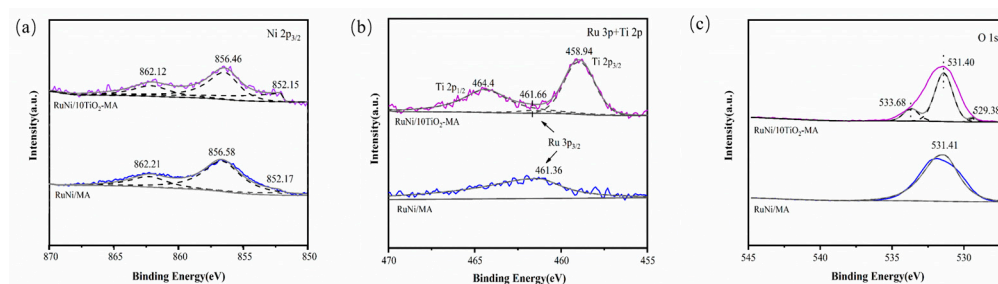
Figure 6. XPS spectra of the (**a**) Ni 2p$_{3/2}$, (**b**) Ru 3p and Ti 2p, and (**c**) O 1s regions for the Ru-Ni/MA and Ru-Ni/10TiO$_2$-MA catalysts.

In this work, the suitable operating temperature window (SOTW) for CO-SMET was defined as a CO outlet concentration below 10 ppm and a reaction selectivity greater than 50% [61]. The effects of different Ti content doping on the performance of the Ru-Ni/MA and Ru-Ni/xTiO$_2$-MA catalysts with different TiO$_2$ loadings (x = 5%,10%, 15%) for CO-SMET were investigated, as displayed in Figure 7. For all Ru-Ni/xTiO$_2$-MA catalysts, with the increase in reaction temperature, the outlet concentration of CO at the outlet of the reactor exhibited a rapid decline to less than 10 ppm, and then a slow rise to more than 10 ppm, but the selectivity of the catalyst presented a monotonically decreasing trend because high temperature was conducive to the CO$_2$ competitive methanation reaction and reverse water-gas shift reaction. The Ru-Ni/TiO$_2$ catalyst shows the lowest catalytic activity; the CO in H$_2$-rich gas cannot be removed to less than 10 ppm. For the Ru-Ni/MA catalyst, the CO concentration could be reduced to less than 10 ppm at the reaction temperature of 220 °C, and its SOWT was about 220–272 °C. Compared with Ru-Ni /MA, the low-temperature catalytic performance of Ru-Ni/xTiO$_2$-MA catalysts was significantly promoted; the SOTW was obviously shifted to a lower temperature and widened after the introduction of TiO$_2$. Among them, the Ru-Ni/10TiO$_2$-MA catalyst shows the superior catalytic activity with a SOTW of 210–280 °C. This can be attributed to the formation of optimal metal–support interaction for Ru-Ni/10TiO$_2$-MA, which promoted the high dispersion of the active components. Moreover, the increase in defective oxygen and surface acidity in the catalyst improved the adsorption and activation of CO, leading to the enhancement of the reaction activity [62]. When the TiO$_2$ content was increased to 15%, the SOTW of the catalyst was reduced to about 210–260 °C, which might be due to the fact that the excess addition of TiO$_2$ clogged the pore channels of the MA, reducing its specific surface area and pore volume, which led to the reduction of active centers, thus resulting in a decrease in catalytic activity [63]. In summary, a TiO$_2$-modified MA support followed by Ru-Ni bimetallic loading can significantly improve the performance of a Ru-Ni/xTiO$_2$-MA catalyst, and when the loading content of TiO$_2$ is 10%, the Ru-Ni/10TiO2-MA catalyst exhibited excellent CO-SMET performance, which can eliminate CO in the H$_2$-rich gas to less than 10 ppm in the temperature window of 210–280 °C and maintain its selectivity above 50%.

The stability test results of the CO-selective methanation reaction over the Ru-Ni/10TiO$_2$-MA catalyst under specific reaction conditions (210 °C, 0.1 MPa, WHSV = 6000 mL·g^{-1}·h^{-1}) are displayed in Figure 8. The CO outlet concentration was maintained at about 3×10^{-6} and the reaction selectivity was higher than 95% during the continuous stability test of 80 h. The excellent stability exhibited by the catalyst was attributed to the fact that the addition of TiO$_2$ improved the metal–support interactions, facilitated the active components' dispersion, and inhibited the sintering agglomeration of active components under prolonged reaction conditions [64].
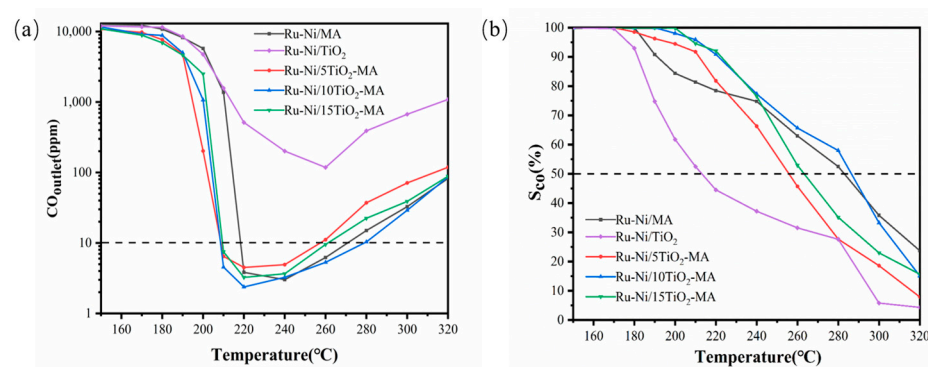
Figure 7. The outlet CO concentration (**a**) and the selectivity of CO methanation (**b**) over the Ru-Ni/TiO$_2$ and Ru-Ni/xTiO$_2$-MA (x = 0, 5%,10%,15%) catalysts for CO-SMET.
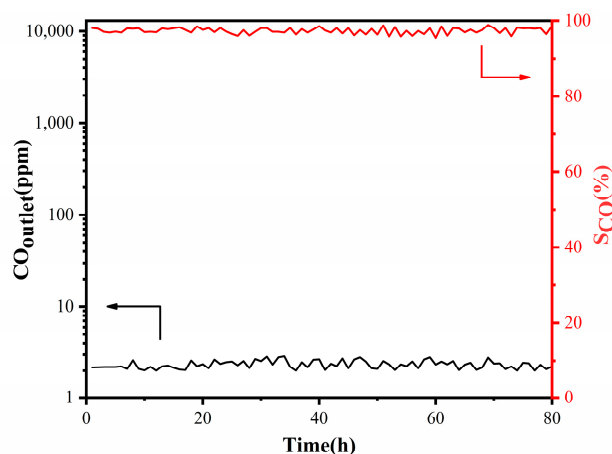
Figure 8. Long-term durability test for CO-SMET over the Ru-Ni/10TiO$_2$-MA catalyst at 210 °C.

3. Materials and Methods

3.1. Materials

All raw materials, i.e., MgCl$_2$·6H$_2$O, AlCl$_3$, NaOH, NaAlO$_2$, C$_9$H$_{21}$AlO$_3$, Mg(NO$_3$)$_2$·6H$_2$O, C$_{16}$H$_{36}$O$_4$Ti, NiCl$_2$·6H$_2$O, and RuCl$_3$·nH$_2$O, were of analytical grade and used without further purification.

3.2. Catalyst Preparation

The MA (MgAl$_2$O$_4$) supports were prepared by a modified co-precipitation method and then loaded with TiO$_2$ by impregnation. Firstly, 6.1 g MgCl$_2$·6H$_2$O and 2.0 g AlCl$_3$ were dissolved in 50 mL deionized water and stirred for 20 min at room temperature to form solution A. Amounts of 2 g NaOH and 1.2 g NaAlO$_2$ were dissolved in 50 mL deionized water and stirred for 20 min at room temperature to form solution B. A total of 2.5 g NaAlO$_2$ was dissolved in 50 mL deionized water and stirred for 20 min at room temperature to form solution C. Subsequently, solution C was transferred into a three-necked flask with a water bath heated at 80 °C. Under stirring, solution A and B were added simultaneously and slowly into solution C in N$_2$ atmosphere. Then 0.2 M NaOH solution was added to the above solution drop by drop until the pH of the solution was 10. The obtained solution was stirred at high speed for another 20 min. The precipitate was filtered, washed with deionized water until the pH value reached 7, dried at 100 °C for 24 h, and subsequently calcinated at 500 °C in a muffle furnace for 3 h to obtain MA.

The xTiO$_2$-MA composite supports were synthesized by means of the impregnation method, where the x represents the mass percent of titanium oxide. Briefly, 0.2 mL tetra-butyl titanate was dissolved in 5 mL anhydrous ethanol with stirring, then 0.5 g MA was

impregnated therein. The obtained suspension was stirred thoroughly in air at room temperature for 10 h. Then the product was dried at 110 °C for 10 h, calcinated at 500 °C in a muffle furnace for 6 h to obtain 10TiO$_2$-MA composite supports with a titanium oxide mass content of 10%. xTiO$_2$-MA composite supports (x = 5%, 15%) were prepared the same way as above by adjusting the tetrabutyl titanate.

The Ru-Ni/xTiO$_2$-MA samples were prepared by the co-impregnation method. Amounts of 0.3 g NiCl$_2$·6H$_2$O and 0.015 g RuCl$_3$·nH$_2$O were dissolved in 10 mL anhydrous ethanol with stirring, then 0.3 g xTiO$_2$-MA was impregnated therein. The obtained suspension was continuously stirred at room temperature for 12 h, then evaporated with slow stirring in a water bath at 80 °C, dried at 100 °C for 12 h, then calcinated in a muffle furnace at 400 °C for 3 h, and reduced under a H$_2$/N$_2$ gas mixture containing H$_2$ 33 vol% at 400 °C for 2 h. The final product is the Ru-Ni/xTiO$_2$-MA with a loading content of 15% Ni and 1.5% Ru (x = 0, 5%, 10%, 15%). The actual loading of Ni and Ru in the catalyst was determined by inductively coupled plasma optical emission spectrometry (ICP-OES). The results showed that the loading of Ni and Ru in the Ru-Ni/10TiO$_2$-MA sample was 14.16% and 1.31%, respectively.

3.3. Catalyst Characterization

The purity of the gases involved in the following characterizations (Ar, CO, N$_2$, NH$_3$) was 99.999%.

The crystal structures of samples were recorded by powder X-ray diffraction (XRD) on a Bruker D8 ADVANCE (Berlin, Germany) X-ray diffractometer with Cu Kα radiation (λ = 0.154 nm), operating at a current of 40 mA and a voltage of 40 kV. The scanning range was set between 5 and 90°. Powder samples of 50 mg were smeared uniformly onto a sample holder to ensure a flat upper surface before the test.

The specific surface area, pore size, and pore volume of the catalysts were measured using a Micromeritics TriStar II 3020 (Micromeritics Instrument Corporation, Norcross, GA, USA) fully automated physical adsorbent meter. The nitrogen adsorption–desorption process was executed at −196 °C. Before testing, the samples underwent degassing and pretreatment at 150 °C for 12 h. The specific surface area was determined using the BET method, and the pore size distribution was calculated by the Barrer–Joyner–Halenda (BJH) equation.

The hydrogen temperature-programmed reduction (H$_2$-TPR) test was carried out using a Micromeritics AutoChem II 2920 (Micromeritics, USA) multifunctional chemisorbent. Before the test, 0.1 g samples were pretreated at 300 °C in Ar gas for 1.5 h to purify their surfaces. After cooling to 50 °C, 10 vol% H$_2$/N$_2$ mixed gas was introduced at a flow rate of 30 mL·min^{-1}, and then the temperature was ramped from 50 °C to 700 °C at a heating rate of 10 °C·min^{-1}. The signal of the H$_2$ that was used for the catalyst reduction was detected with TCD and, finally, the H$_2$-TPR curve was obtained.

The carbon monoxide temperature-programmed desorption (CO-TPD) test was conducted on a BELCAT-A automated chemical adsorption instrument (MicrotracBEL Inc., Tokyo, Japan) and TCD was used as the detector. Firstly, 0.1 g samples of the catalyst were weighed to place in the quartz tube, heated to 400 °C from room temperature at a heating rate of 10 °C·min^{-1} and reduced at 50 vol% H$_2$/N$_2$ atmosphere at a flow rate of 60 mL·min^{-1} for 2 h. When the reduction was over, He gas was switched to the quartz tube at a flow rate of 30 mL·min^{-1}. After the sample was cooled down to 50 °C, a CO atmosphere with a flow rate of 30 mL·min^{-1} was introduced for 1 h to saturate the sample with CO adsorption. Subsequently, He gas was purged at a flow rate of 30 mL·min^{-1} for 1 h to remove the weak physical adsorption CO on the sample surface. When the baseline signal corresponded to the TCD, the temperature was ramped up from room temperature

to 800 °C at a heating rate of 10 °C·min^{-1} in He atmosphere. The signal of the CO that was desorbed on the catalyst during this process was detected.

The ammonia temperature-programmed desorption (NH$_3$-TPD) test was carried out using the BELCAT-A automated chemical adsorption instrument (MicrotracBEL Inc., Tokyo, Japan) and TCD was used as the detector. Briefly, 0.1 g catalyst samples were weighed to place in the reaction tube, and reduced in a 10 vol% H$_2$/N$_2$ atmosphere with a flow rate of 60 mL·min^{-1} at 400 °C for 3 h. Then, He gas was switched to the quartz tube at a flow rate of 30 mL·min^{-1}. After the temperature was lowered below 50 °C, NH$_3$ was introduced at a flow rate of 30 mL·min^{-1} and maintained for 1 h to saturate the sample with NH$_3$ adsorption. Following this process, He gas was purged at a flow rate of 30 mL·min^{-1} for 1 h. When the baseline signal corresponding to the mass spectrum stabilized, the temperature was ramped up from room temperature to 800 °C at a heating rate of 10 °C·min^{-1}. The signal of NH$_3$ desorbed on the catalyst during this process was detected.

The microstructure of the catalysts was observed by a HITACHI SU-8220 (Tokyo, Japan) high-resolution field scanning electron microscope (SEM) equipped with an energy dispersive x-ray spectrometer (EDS). Prior to the test, a small amount of sample was dispersed by ultrasonication with drops of anhydrous ethanol, then a small amount of the solution was pipetted onto a special silicon wafer and dried in a fume hood at room temperature. Finally, the dried wafer was sprayed with gold, and put into the sample stage of the instrument to be fixed and tested.

Transmission electron microscopy (TEM) and high-resolution transmission electron microscopy (HRTEM) images were obtained using a JEOL JEM-2100F transmission electron microscope (Tokyo, Japan). During the test, the samples were uniformly dispersed in absolute ethanol for 10 min, and a small amount of suspension was applied to the copper grid coated with a carbon film. Subsequently, the samples were subjected to a drying treatment.

The surface chemical states of catalysts were analyzed by X-ray photoelectron spectroscopy (XPS) using Al-Kα X-ray source (hv = 1486.6 eV) from a Kratos Axis Supra+ photoelectron spectrometer (Kratos Analytical Ltd., Manchester, UK). The binding energy of carbon C 1s (284.8 eV) on the sample surface was used as the internal standard for calibration, using the software Avantage (5.9) to perform split-peak fitting. Before the test, powder samples were securely fixed on a sample stage using a conductive adhesive. The non-adhered powder was removed by gently blowing with an ear wash ball.

The contents of Ni and Ru in the Ru-Ni/ 10TiO$_2$-MgAl$_2$O$_4$ catalyst were assessed using Agilent 5110 ICP-OES (Agilent Technologies Inc., Santa Clara, CA, USA). The sample was digested in an HF aqueous solution before measurement.

3.4. Catalyst Activity Evaluation

The CO-SMET reaction was carried out in a fixed-bed quartz tubular reactor with an inner diameter of 6 mm, an outer diameter of 10 mm, and a length of 300 mm at atmospheric pressure. The reactor was loaded with about 200 mg of catalyst with a particle size of 40–60 mesh. During the experiment, the catalyst was firstly heated up to 80 °C in N$_2$ atmosphere. Then the reactor was fed with 50 vol% N$_2$/H$_2$ mixture gas at the flowrate of 60 mL·min^{-1} and heated up to 400 °C for 2 h. After the temperature of the catalyst bed was cooled to 150 °C, the hydrogen-rich gas (1.01 vol% CO/20.5 vol% CO$_2$/ 78.49 vol% H$_2$) was switched to the reactor at the flowrate of 20 mL·min-1. The effluents from the reactor were analyzed using an online Agilent 7820A gas (Agilent Technologies Inc., California, USA) chromatograph equipped with a flame ionization detector (FID) and a thermal conductivity detector (TCD), and a packed column (TDX-01). The catalytic activity was evaluated based

on the CO concentration in the effluent [65,66]. The CO selectivity (SCO) of the catalyst was calculated by the following formula:

$$S_{CO} = \frac{F_{CO}^{inlet} - F_{CO}^{outlet}}{F_{CH_4}^{outlet}} \times 100\%$$

where F_{CO}^{inlet} is the CO concentration in feedstock gases, mmol·min^{-1}, and F_{CO}^{outlet} and $F_{CH_4}^{outlet}$ are the concentrations of CO and CH$_4$ in effluent gases, respectively, mmol·min^{-1}.

4. Conclusions

In summary, surface titanium-modified MgAl$_2$O$_4$-loaded Ru-Ni bimetallic catalysts were successfully synthesized. The results showed that the Ru-Ni/10TiO$_2$-MA catalyst demonstrated the superior catalytic activity for the selective methanation reaction of CO in hydrogen-rich gases with the suitable operating temperature window of (210–280 °C). The addition of TiO$_2$ can effectively lower the reduction temperature of the active component Ni, thus increasing the high dispersion of active component. Moreover, the interaction mode between the active metal and the support was improved and the acidity on the catalyst surface was enhanced, which facilitates the adsorption and activation of CO to promote the reaction. This study provides a new strategy for designing efficient CO-SMET catalysts.

Supplementary Materials: The following supporting information can be downloaded at: https://www.mdpi.com/article/10.3390/catal15010018/s1, Figure S1: XRD patterns of the MA and xTiO$_2$-MA supports; Figure S2: (a) N$_2$ adsorption–desorption isotherms and (b) pore size distributions of the samples; Figure S3: SEM images of (a) MA, (b) 5TiO$_2$-MA, (c) 10TiO$_2$-MA, and (d) 15TiO$_2$-MA; Table S1: Structural properties of the samples; Table S2: The particle size of Ni estimated by Scherrer equation of the samples. Table S3: The H$_2$-TPR Guass fitting analysis of the samples.

References

1. Sengodan, S.; Lan, R.; Humphreys, J.; Du, D.; Xu, W.; Wang, H.; Tao, S. Advances in Reforming and Partial Oxidation of Hydrocarbons for Hydrogen Production and Fuel Cell Applications. *Renew. Sust. Energ. Rev.* **2018**, *82*, 761–780. [CrossRef]
2. Zyryanova, M.M.; Snytnikov, P.V.; Gulyaev, R.V.; Amosov, Y.I.; Boronin, A.I.; Sobyanin, V.A. Performance of Ni/CeO$_2$ Catalysts for Selective CO Methanation in Hydrogen-Rich Gas. *Chem. Eng. J.* **2014**, *238*, 189–197. [CrossRef]
3. Trimm, D.L. Minimisation of Carbon Monoxide in a Hydrogen Stream for Fuel Cell Application. *Appl. Catal. A Gen.* **2005**, *296*, 1–11. [CrossRef]
4. Specchia, S.; Galletti, C.; Saracco, G.; Specchia, V. Final CO Clean-Up Step of Reformate Gases Via Methanation Process. *ECS Tran.* **2008**, *12*, 579–587. [CrossRef]
5. Wang, K.; Men, Y.; Liu, W.; Zhang, J.K. Recent Progress in Catalytical CO$_2$ Purification of H-rich Reformate for Proton Exchange Membrane Fuel Cells. *Int. J. Hydrogen Energy* **2023**, *48*, 25100–25118. [CrossRef]
6. Liu, B.; Yao, N.; Li, S.; Wang, J.; Lv, D.Y.; Li, X.N. Methanation of CO in Hydrogen-Rich Gas on Ni-Ru/SiO$_2$ Catalyst: The Type of Active Sites and Ni-Ru Synergistic Effect. *Chem. Eng. J.* **2016**, *304*, 476–484. [CrossRef]
7. Tada, S.; Minori, D.; Wada, K.; Osada, K.; Akiyama, K.; Satokawa, S.; Kawashima, Y. Long-Term Durability of Ni/TiO$_2$ and Ru-Ni/TiO$_2$ Catalysts for CO Selective Methanation. *J. Power. Sources* **2014**, *264*, 59–66. [CrossRef]

8. Chen, A.H.; Miyao, T.; Higashiyama, K.; Yamashita, H.; Watanabe, M. High Catalytic Performance of Ruthenium-Doped Mesoporous Nickel-Aluminum Oxides for Selective CO Methanation. *Angew. Chem. Int. Ed.* **2010**, *122*, 10091–10094. [CrossRef]

9. Tada, S.; Kikuchi, R.; Takagaki, A.; Sugawara, T.; Oyama, S.T.; Urasaki, K.; Satokawa, S. Study of Ru-Ni/TiO$_2$ Catalysts for Selective CO Methanation. *Appl. Catal. B* **2013**, *140–141*, 258–264. [CrossRef]

10. Tada, S.; Minori, D.; Otsuka, F.; Kikuchi, R.; Osada, K.; Akiyama, K.; Satokawa, S. Effect of Ru and Ni Ratio on Selective CO methanation over Ru-Ni/TiO$_2$. *Fuel* **2014**, *129*, 219–224. [CrossRef]

11. Dai, X.P.; Liang, J.; Ma, D.; Zhang, X.; Zhao, H.B.; Zhao, B.; Guo, Z.G.; Kleita, F.; Qiao, S.Z. Large-Pore Mesoporous RuNi-doped TiO$_2$-Al$_2$O$_3$ Nanocomposites for Highly Efficient Selective CO Methanation in Hydrogen-rich Reformate Gases. *Appl. Catal. B* **2015**, *165*, 752–762. [CrossRef]

12. Yang, K.W.; Zhang, M.H.; Yu, Y.Z. Effect of Transition Metal-doped Ni(211) for CO Dissociation: Insights from DFT Calculations. *Appl. Surf. Sci.* **2017**, *399*, 255–264. [CrossRef]

13. Di Cosimo, J.I.; Díez, V.K.; Xu, M.; Iglesia, E.; Apestguía, C.R. Structure and Surface and Catalytic Poperties of Mg-Al Basic Oxides. *J. Catal.* **1998**, *178*, 499–510. [CrossRef]

14. Li, W.Z.; Kovarik, L.; Mei, D.; Liu, J.; Wang, Y.; Peden, C.H.F. Stable Platinum Nanoparticles on Specific MgAl$_2$O$_4$ Spinel Facets at High Temperatures in Oxidizing Atmospheres. *Nat. Commun.* **2013**, *4*, 2481. [CrossRef]

15. Wang, F.; Li, W.Z.; Lin, J.D.; Chen, Z.Q.; Wang, Y. Crucial Support Effect on the Durability of Pt/MgAl$_2$O$_4$ for Partial Oxidation of Methane to Syngas. *Appl. Catal. B* **2018**, *231*, 292–298. [CrossRef]

16. Ren, G.Q.; Pei, G.X.; Ren, Y.J.; Liu, K.P.; Chen, Z.Q.; Yang, J.Y.; Su, Y.; Liu, X.Y.; Li, W.Z.; Zhang, T. Effect of Group IB Metals on the Dehydrogenation of Propane to Propylene over Anti-sintering Pt/MgAl$_2$O$_4$. *J. Catal.* **2018**, *366*, 115–126. [CrossRef]

17. Baek, S.C.; Jun, K.W.; Lee, Y.J.; Kim, J.D.; Park, D.Y.; Lee, K.Y. Ru/Ni/MgAl$_2$O$_4$ Catalysts for Steam Reforming of Methane: Effects of Ru Content on Self-Activation Property. *Res. Chem. Intermed.* **2012**, *38*, 1225–1236. [CrossRef]

18. Andraos, S.; Abbas-Ghaleb, R.; Chlala, D.; Vita, A.; Italiano, C.; Laganà, M.; Pino, L.; Nakhl, M.; Specchia, S. Production of Hydrogen by Methane Dry Reforming over Ruthenium-Nickel Based Catalysts Deposited on Al$_2$O$_3$, MgAl$_2$O$_4$, and YSZ. *Int. J. Hydrogen Energy* **2019**, *44*, 25706–25716. [CrossRef]

19. Navarro, J.C.; Centeno, M.A.; Laguna, O.H.; Odrizola, J.A. Ru–Ni/MgAl$_2$O$_4$ Structured Catalyst for CO$_2$ Methanation. *Renew. Energ.* **2020**, *161*, 120–132. [CrossRef]

20. Singha, R.K.; Shukla, A.; Sandupatla, A.; Deo, G.; Bal, R. Synthesis and Catalytic Activity of A Pd Doped Ni-MgO Catalyst for Dry Reforming of Methane. *J. Mater. Chem. A* **2017**, *5*, 15688–15699. [CrossRef]

21. Sreenavya, A.; Ahammed, S.; Ramachandran, A.; Ganesh, V.; Sakthivel, A. Nickel-Ruthenium Bimetallic Species on Hydrotalcite Support: A Potential Hydrogenation Catalyst. *Catal. Lett.* **2022**, *152*, 848–862. [CrossRef]

22. Prescott, H.; Li, Z.; Kemnitz, E.; Deutsch, J.; Lieske, H.; Auroux, A. Application of Calcined Mg-Al Hydrotalcites for Michael Additions: An Investigation of Catalytic Activity and Acid-Base Properties. *J. Catal.* **2005**, *234*, 119–130. [CrossRef]

23. Nematollahi, B.; Rezaei, M.; Amini, E.; Lay, E.N. Preparation of High Surface Area Ni/MgAl$_2$O$_4$ Nanocatalysts for CO Selective Methanation. *Int. J. Hydrogen Energy* **2018**, *43*, 772–780. [CrossRef]

24. Wang, S.J.; Tian, Z.W.; Liu, Q.; Qiao, Y.Y.; Tian, Y.Y. Facile Preparation of A Ni/MgAl$_2$O$_4$ Catalyst with High Surface Area: Enhancement in Activity and Stability for CO Methanation. *Main Group Met. Chem.* **2018**, *41*, 73–89. [CrossRef]

25. Tsipouriari, V.A.; Efstathiou, A.M.; Zhang, Z.L.; Verykios, X.E. Reforming of Methane with Carbon Dioxide to Synthesis Gas Over Supported Rhodium Catalysts. *J. Catal.* **1996**, *158*, 51–63.

26. Shah, M.; Bordoloi, A.; Nayak, A.K.; Mondal, P. Effect of Ti/Al Ratio on the Performance of Ni/TiO$_2$-Al$_2$O$_3$ Catalyst for Methane Reforming with CO$_2$. *Fuel Process. Technol.* **2019**, *192*, 21–35. [CrossRef]

27. Lim, J.; Kim, Y.; Kim, S.; Kim, Y.; Kang, S. Defects on the Surface of Ti-Doped MgAl$_2$O$_4$ Nanophosphor. *Nanoscale Res. Lett.* **2017**, *12*, 536. [CrossRef]

28. Kong, L.; Ma, J.; Huang, H. MgAl$_2$O$_4$ Spinel Phase Derived Fromoxide Mixture Activated by a High-Energy Ball Milling Process. *Mater. Lett.* **2002**, *56*, 238–243. [CrossRef]

29. Jouini, A.; Sato, H.; Yoshikawa, A.; Fukuda, T.; Boulon, G.; Panczer, G.; Kato, K.; Hanamura, E. Ti-Doped MgAl$_2$O$_4$ Spinel Single Crystals Grown by the Micro-Pulling-Down Method for Laser Application: Growth and Strong Visible Blue Emission. *J. Mater. Res.* **2006**, *21*, 2337–2344. [CrossRef]

30. Zhang, H.K.; Wang, W.C.; Xiang, Z.Y.; Zhou, F.Y.; Zhu, W.B.; Wang, H.L. Ni Supported on Ti-Doped SBA-15 Catalyst for the Selective Hydrodeoxygenation Conversion of Lignin Derivatives. *J. Fuel Chem. Technol.* **2024**, *52*, 536–544. [CrossRef]

31. Muttakin, M.; Mitra, S.; Thu, K.; Ito, K.; Saha, B.B. Theoretical Framework to Evaluate Minimum Desorption Temperature for IUPAC Classified Adsorption Isotherms. *Int. J. Heat Mass Transf.* **2018**, *122*, 795–805. [CrossRef]

32. Shimoda, N.; Fujiwara, M.; Tani, K.; Shoji, D.; Takahashi, M.; Akiyama, K.; Satokawa, S. Durability of Ni/TiO$_2$ Catalyst Containing Trace Chlorine for CO Selective Methanation. *Appl. Catal. A Gen.* **2018**, *557*, 7–14. [CrossRef]

33. Alihosseinzadeh, A.; Nematollahi, B.; Rezaei, M.; Lay, E.N. CO Methanation over Ni Catalysts Supported on High Surface Area Mesoporous Nanocrystalline γ-Al$_2$O$_3$: For CO Removal in H$_2$-Rich Stream. *Int. J. Hydrogen Energy* **2015**, *40*, 1809–1819. [CrossRef]

34. Abdel-mageed, A.M.; Widmann, D.; Olesen, S.E.; Chorkendorff, I.; Biskupek, J.; Behm, R.J. Selective CO Methanation on Ru/TiO$_2$ Catalysts: Role and Influence of Metal Support Interactions. *ACS Catal.* **2015**, *5*, 6753–6763. [CrossRef]

35. Heo, Y.-J.; Park, S.-J. Facile Synthesis of MgO-Modified Carbon Adsorbents with Microwave- Assisted Methods: Effect of MgO Particles and Porosities on CO$_2$ Capture. *Sci. Rep.* **2017**, *7*, 5653. [CrossRef]

36. Liu, J.; Yu, J.; Su, F.B.; Xu, G.W. Intercorrelation of Structure and Performance of Ni-Mg/Al$_2$O$_3$ Catalysts Prepared with Different Methods for Syngas Methanation. *Catal. Sci. Technol.* **2014**, *4*, 472–481. [CrossRef]

37. Nematollahi, B.; Rezaei, M.; Lay, E.N. Preparation of Highly Active and Stable NiO-CeO$_2$ Nanocatalysts for CO Selective Methanation. *Int. J. Hydrogen Energy* **2015**, *40*, 8539–8547. [CrossRef]

38. Liu, J.; Li, C.M.; Wang, F.; He, S.; Chen, H.; Zhao, Y.F.; Wei, M.; Evans, D.G.; Duan, X. Enhanced Low-Temperature Activity of CO$_2$ Methanation over Highly-Dispersed Ni/TiO$_2$ Catalyst. *Catal. Sci. Technol.* **2013**, *3*, 2627–2633. [CrossRef]

39. Zhu, C.; Cao, J.P.; Zhao, X.Y.; Xie, T.; Zhao, M.; Wei, X.Y. Bimetallic Effects in the Catalytic Hydrogenolysis of Lignin and its Model Compounds on Nickel-Ruthenium Catalysts. *Fuel Process. Technol.* **2019**, *194*, 106–126. [CrossRef]

40. Pan, Y.X.; Liu, C.J.; Shi, P. Preparation and Characterization of Coke Resistant Ni/SiO$_2$ Catalyst for Carbon Dioxide Reforming of Methane. *J. Power Sources* **2008**, *176*, 46–53. [CrossRef]

41. Foppa, L.; Lannuzzi, M.; Copéret, C.; Comas-Vives, A. CO Methanation on Ruthenium Flat and Stepped Surfaces: Key Role of H-transfers and Entropy Revealed by ab Initio Molecular Dynamies. *J. Catal.* **2019**, *371*, 270–275. [CrossRef]

42. Kim, Y.; Lim, J.; Kang, S. Thermodynamic Investigation of Ti Doping in MgAl$_2$O$_4$ Based on the First-Principles Method. *J. Mater. Chem. C* **2015**, *3*, 8970–8978. [CrossRef]

43. Mohaideen, K.K.; Kim, W.; Koo, K.Y.; Yoon, W.L. Highly Dispersed Ni Particles on Ru/NiAl Catalyst Derived from Layered Double Hydroxide for Selective CO Methanation. *Catal. Commun.* **2015**, *60*, 8–13. [CrossRef]

44. Yadav, M.; Mishra, D.K.; Hwang, J. Catalytic Hydrogenation of Xylose to Xylitol Using Ruthenium Catalyst on NiO Modifed TiO$_2$ Support. *Appl. Catal. A Gen.* **2012**, *425–426*, 110–116. [CrossRef]

45. Ping, D.; Dong, X.F.; Zang, Y.H.; Feng, X. Highly Efficient MOF-Templated Ni Catalyst Towards CO Selective Methanation in Hydrogen-Rich Reformate Gases. *Int. J. Hydrogen Energy* **2017**, *42*, 15551–15556. [CrossRef]

46. Jhang, J.H.; Schaefer, A.; Zielasek, V.; Weaver, J.; Bäumer, M. Methanol Adsorption and Reaction on Samaria Thin Films on Pt(111). *Materials* **2015**, *8*, 6228–6256. [CrossRef]

47. Liu, Q.; Zhong, Z.; Gu, F.; Wang, X.; Lu, X.; Li, H.; Xu, G.; Su, F. CO Methanation on Ordered Mesoporous Ni–Cr–Al Catalysts: Effects of the Catalyst Structure and Cr Promoter on the Catalytic Properties. *J. Catal.* **2016**, *337*, 221–232. [CrossRef]

48. Narasimharao, K.; Seetharamulu, P.; Rao, K.R.; Basahel, S.N. Carbon Covered Mg-Al Hydrotalcite Supported Nanosized Ru Catalysts for Ammonia Synthesis. *J. Mol. Catal. A Chem.* **2016**, *411*, 157. [CrossRef]

49. Burch, R.; Flambard, A.R. Strong Metal-Support Interactions in Nickel/Titania Catalysts: The Importance of Interfacial Phenomena. *J. Catal.* **1982**, *78*, 389–405. [CrossRef]

50. Shaaban, E.; Li, G. Probing Active Sites for Carbon Oxides Hydrogenation on Cu/TiO$_2$ Using Infrared Spectroscopy. *Commun. Chem.* **2022**, *5*, 32. [CrossRef]

51. Martra, G. Lewis Acid and Base Sites at the Surface of Microcrystalline TiO$_2$ Anatase: Relationships between Surface Morphology and Chemical Behaviour. *Appl. Catal. A Gen.* **2000**, *200*, 275–285. [CrossRef]

52. Zhang, J.Y.; Xin, Z.; Meng, X.; Lv, Y.H.; Tao, M. Effect of MoO$_3$ on Structures and Properties of Ni-SiO$_2$ Methanation Catalysts Prepared by the Hydrothermal Synthesis Method. *Ind. Eng. Chem. Res.* **2013**, *52*, 14533–14544. [CrossRef]

53. Wang, J.; Yuan, C.K.; Yao, N.; Li, X.N. Effect of the Nanostructure and the Surface Composition of Bimetallic Ni-Ru Nanoparticles on the Performance of CO Methanation. *Appl. Surf. Sci.* **2018**, *441*, 816–823. [CrossRef]

54. Chen, Y.; Wu, M.; Li, J.; Zhao, Q.; Zhang, S.; Guo, Y.; Feng, F.; Li, Z. Study on the Hydrogen Evolution Performance of RuNi/TiO$_2$-oxMWCNT Catalyst in Alkaline Media. *Colloids Surf. A Physicochem. Eng. Asp.* **2023**, *678*, 132514. [CrossRef]

55. Shi, X.; Chen, J.; Ke, K.; Gan, X.; Yang, M.; Xiong, K. Metal/Metal Oxide Modulation of RuNi Catalysts on TiO$_2$ Nanosheets Promoting Overall Water Splitting. *ACS Appl. Nano Mater.* **2024**, *7*, 27309–27317. [CrossRef]

56. Chen, H.; He, S.; Cao, X.Z.; Zhang, S.T.; Xu, M.; Pu, M.; Su, D.S.; Wei, M.; Evans, D.G.; Duan, X. Ru-Cluster-Modified Ni Surface Sefects toward Selective Bond Breaking between C–O and C–C. *Chem. Mater.* **2016**, *28*, 4751–4761. [CrossRef]

57. Xu, M.; He, S.; Chen, H.; Cui, G.Q.; Zheng, L.R.; Wang, B.; Wein, M. TiO$_{2-x}$-Modified Ni Nanocatalyst with Tunable Metal-Support Interaction for Water-Gas Shift Reaction. *ACS Catal.* **2017**, *7*, 7600–7609. [CrossRef]

58. Gutièrrez, A.A.; Ramirez, J.; Val, I.J. Activity of NiW Catalysts Supported on TiO$_2$-Al$_2$O$_3$ Mixed Oxides: Effect of Ti Incorporation Method on the HDS of 4,6-DMDBT. *Catal. Today* **2005**, *107–108*, 879–884. [CrossRef]

59. Sui, D. Atomic Ruthenium Doping in Collaboration with Oxygen Vacancy Engineering Boosts the Hydrogen Evolution Reaction by Optimizing H Absorption. *Chem. Eng. J.* **2024**, *480*, 148007. [CrossRef]

60. Meng, W.; Song, X.; Bao, L.; Chen, B.; Ma, Z.; Zhou, J.; Jiang, Q.; Wang, F.; Liu, X.; Shi, C.; et al. Synergistic Doping and De-Doping of Co$_3$O$_4$ Catalyst for Effortless Formaldehyde Oxidation. *Chem. Eng. J.* **2024**, *494*, 153028. [CrossRef]

61. Ping, D.; Dong, C.; Zhao, H.; Dong, X.F. A Novel Hierarchical RuNi/Al$_2$O$_3$ –Carbon Nanotubes/Ni Foam Catalyst for Selective Removal of CO in H$_2$ -Rich Fuels. *Ind. Eng. Chem. Res.* **2018**, *57*, 5558–5567. [CrossRef]

62. Rosha, P.; Mohapatra, S.K.; Mahla, S.K.; Dhir, A. Biogas Reforming for Hydrogen Enrichmet by Ceria Decorated over Nickel Catalyst Supported on Titania and Alumina. *Int. J. Hydrogen Energy* **2018**, *43*, 21246–21255. [CrossRef]

63. Mishra, D.K.; Lee, J.; Chang, J.; Hwang, J. Liquid Phase Hydrogenation of D-glucose to D-sorbitol over the Catalyst (Ru/NiO-TiO$_2$) of Ruthenium on a NiO-Modified TiO$_2$ Support. *Catal. Today* **2012**, *185*, 104–108. [CrossRef]

64. Chen, S.L.; Abdel-Mageed, A.M.; Gauckler, C.; Olesen, S.E.; Chorkendorff, I.; Behm, R.J. Selective CO Methanation on Isostructural Ru Nanocatalysts: The Role of Support Effects. *J. Catal.* **2019**, *373*, 103–115. [CrossRef]

65. Ping, D.; Dong, X.F.; Zang, Y.H.; Feng, X. Highly Efficient Ru/TiO$_2$-NiAl Mixed Oxide Catalysts for CO Selective Methanation in Hydrogen-Rich Gas. *Int. J. Energy Res.* **2017**, *41*, 2308–2317. [CrossRef]

66. Shi, Z.; Feng, J.; Dong, X.F. Ru–Ni/GA-MMO Composites as Highly Active Catalysts for CO Selective Methanation in H$_2$-Rich Gases. *Int. J. Hydrogen Energy* **2023**, *48*, 24640–24651. [CrossRef]